JOURNAL OF AIRCRAFT
Vol. 38, No. 2, March–April 2001

Aerodynamic Simulations of Airfoils with Upper-Surface Ice-Shapes

Satish Kumar* and Eric Loth†
University of Illinois at Urbana, Champaign, Urbana, Illinois 61801

A computational investigation was conducted to determine the effect of simulated upper-surface spanwise ice shapes on airfoil aerodynamics. These shapes are representative of supercooled large droplet shapes on aircraft with active de-icing boots. The numerical investigation employed steady-state simulations with a high-resolution full Navier–Stokes solver using a solution-adaptive unstructured grid for both non-iced and iced configurations. The study investigated a modified NACA 23012 (with and without flap deflection) and airfoils of the NASA Modern Airfoil program. A range of protuberance location, size, and shape were examined, and comparisons were made to available experimental data. In general, the performance of the computational methodology was particularly good for pressure and hinge-moment distributions (including the nonlinear break points), whereas lift was predicted reasonably well up to (but not past) fully separated flow conditions. The airfoil shape sensitivity studies indicated that the NACA 23012m exhibited the most detrimental performance with respect to lift loss, which tended to be greatest around x/c of about 0.1 that also corresponds to the location of minimum C_p. The more evenly loaded NLF 0414 airfoil tended to have less separation for equivalent clean-airfoil lift conditions and did not exhibit a unique critical ice-shape location. The forward-loaded airfoils of the business jet main wing model and the commercial transport horizontal tailplane model exhibited critical ice-shape locations close to the leading edge (x/c = 0.02), which was close to the minimum C_p location.

Introduction

AN AIRCRAFT can accrete ice on its aerodynamic surfaces when flying through clouds of supercooled water droplets. In the presence of supercooled large droplets, the droplet sizes are much larger than those in the FAA Part 25, Appendix C icing envelopes used in aircraft certification. Because of their larger size, the droplets can impinge and accrete as ice downstream of the de-icing system. When the de-icing system is activated, a spanwise-step ice accretion can occur on the aircraft wing behind the leading-edge de-icing system.[1] The spanwise-step ice accretion (just behind the boot) presents both a forward and aft facing step to the flow and is essentially two-dimensional, extending spanwise on the wing. This type of accretion, if asymmetric, can lead to large changes in the lateral control (and the associated aileron hinge moments) by severely altering the flow over the ailerons.[2] The purpose of this study is to assess the predictive performance of steady-state two-dimensional numerical simulations of the aerodynamics of spanwise-step ice accretions, with particular emphasis to lift degradation and hinge-moment variation. The second goal was to investigate various parameter effects of the ice-shape size, flap deflection, and airfoil type on these aerodynamic forces.

Similar to previous experimental studies, previous computational studies of aircraft icing have primarily concentrated on the more common leading-edge ice shapes. For example, Potapczuk[3,4] used the ARC2D code to study the aerodynamic effects of leading-edge ice. The ARC2D code solves the thin-layer Navier–Stokes equations, with turbulence simulated with the Baldwin–Lomax algebraic two-layer eddy-viscosity model.[5] One of the geometries studied was a NACA 0012 airfoil with a leading-edge glaze-ice accretion. The lift, drag, and moment computations for angles of attack of 0 to 10 deg showed good agreement for angles of attack below stall, and the predicted pressure distribution showed good agreement for locations aft of the ice shape. Recently, Caruso and Farschi[6] used an unstructured mesh flow code and demonstrated high resolution of the detailed flowfield around a leading-edge iced airfoil. The study focused primarily on the grid-generation procedure, and no comparisons with experiment were given. Dompierre et al.[7] also reported results of computations about iced airfoils using adaptive meshing techniques. An efficient remeshing technology was employed such that the Navier–Stokes equations could be solved on and adapted to a grid with a uniform distribution of error. The computations revealed a very large loss of lift, but no experimental data were available for comparison. Kwon and Sankar[8] studied the flow about a three-dimensional finite wing with simulated leading-edge glaze ice and a NACA 0012 airfoil section. The computational study employed the unsteady three-dimensional Baldwin–Lomax equations on a structured algebraic C grid. Pressure distributions along spanwise locations were presented for 4 and 8 deg, which showed reasonable agreement with experimental data. However, the preceding simulations have been generally limited to leading-edge ice-shape simulations.

One of the few relevant computational studies on large-droplet ice accretion (upper-surface spanwise-step ice shapes) was presented by Wright and Potapczuk.[9] The study used the ARC2D structured Navier–Stokes code with an algebraic turbulence model for a variety of airfoil configurations and ice shapes. Although no experimental data were presented for comparison (as none were available), Mach number contours of the flowfield were presented for each of the cases considered. Recently, extensive experimental data (lift, drag, pitching-moment, hinge-moment, and pressure distribution) for upper-surface spanwise-step-ice accretion shapes became available though the work of Bragg at the University of Illinois.[10,11] In 1999 (Ref. 12) the first detailed comparison of these data with computational predictions was presented with emphasis on ice-shape size and shape for the NACA 23012m airfoil alone. This follow-on study considers ice-shape location, flap deflection effects, and three other airfoil geometries from the NASA John H. Glenn Research Center Modern Airfoil Program. The coordinates for the business jet main wing model and the commercial transport horizontal tailplane model of the NASA Modern Airfoil program are presented in Addy.[13]

Received 31 July 2000; revision received 9 October 2000; accepted for publication 6 November 2000.

*Graduate Research Assistant, Department of Aeronautical and Astronautical Engineering. Student Member AIAA.

†Associate Professor, Department of Aeronautical and Astronautical Engineering. Associate Fellow AIAA.

Methodology

Unstructured Grid Technique

Most aerodynamic simulations using computational fluid dynamics are performed using structured grids. Structured grids are very efficient and are very convenient for conventional airfoil with attached flow. However, many complex geometry features, such as ice accretions and/or multielement airfoils, are not easily mapped onto a conventional structured grid. A solution to this problem is to use unstructured grids as they can provide flexibility for tessellating about complex geometries and adapting to flow features. Generating unstructured grids is also much more automatable than conventional multiblock structured grid generation and significantly reduces the number of nodes required for equivalent spatial resolution especially by employing adaptive meshing.

For this study the unstructured grid generation was accomplished using a modified version of UMESH2D (a code developed by Mavriplis[14]). Grid generation within UMESH2D is separated into two stages. First the viscous mesh is generated, and then the rest of the mesh is filled in. The algorithms used are described in the following sections. The first phase of the grid-generation process uses the advancing-layers method as described by Pirzadeh.[15] This stage creates a highly stretched semistructured grid within the viscous regions around the airfoil geometry and wakes. The second phase of the grid-generation process creates isotropic elements within the inviscid regions of the flowfield. This hybrid technique is essentially an advancing-front algorithm that adds new points ahead of the front and triangulates them using the Delaunay criterion. It therefore combines the efficiency and mathematical elegance of Delaunay triangulation with the point placement features, robustness, and boundary integrity of the advancing-front method. An example of an unstructured grid generated for this study is shown in Fig. 1a, which shows a close up of the leading-edge glaze ice shape on a NACA 0012, where highly resolved viscous regions are easily wrapped around the airfoil along with a pointwise efficient inviscid grid, using a total of about 60,000 grid nodes. The computations were conducted on an SGI Origin 2000 and required approximately 6 CPU hours per node (typically 20 angles were run on 20 nodes).

For the upper-surface ice-shape airfoils investigated in this study, it was found that the predictive performance could be significantly enhanced by employing grid adaptation to allow high resolution in regions of high flow gradients. Although UMESH2D has a general grid adaptivity technique, this was modified to better suit the present application. After an initial unstructured grid has been generated and a flow solution has been obtained on this mesh, an adaptively refined mesh was constructed by adding new points in regions of large flow gradients and discretization errors. The grid refinement was performed herein by splitting edges in regions of high flowfield gradients of a flow variable. If the gradient of a particular flow variable were larger than some prescribed tolerance, the edge was refined by adding a new point at the midpoint of the edge. In this study the grid refinement flow variable was set to be the absolute velocity (based on tests for a variety of parameters and combinations in terms of overall efficiency and performance of the adapted grids).

Figure 1b shows a close up of the adapted grid for one level of grid refinement (typically two were used) near the quarter-round simulated ice shape for $\alpha = 0$ deg. In this grid additional grid points have been clustered around the separation point (at the apex of the shape), along the high velocity gradients of the downstream free shear layer (to the right of the shape apex), and near the upstream separation bubble (to the left of the shape base). After the grid has been refined, a new flowfield solution is obtained on the new adapted grid, which is initialized by interpolation from the already computed solution. This interpolation is accomplished by using an efficient node neighbor search. This process could then be repeated for further refinement. The two levels of adaptation typically used herein increased the number of grid points by approximately 25%.

Flowfield Solution

The flow solution is obtained with a code called NSU2D (Version 5.0.b).[16] This code takes a discretized mesh of the flowfield and obtains a steady-state solution of the governing equations. The detailed methodology used in NSU2D is described in the following sections. The flow solver obtains the steady-state solution of the full two-dimensional compressible Reynolds (Favre)-averaged Navier–Stokes equations without a thin-layer assumption. The code uses a vertex-based discretization where the flow variables are stored at the triangle vertices. The flux terms are evaluated using a Galerkin-based finite element formulation. A blend of Laplacian and biharmonic operators is incorporated for stability. The biharmonic dissipation provides second-order-accurate background diffusion in regions of smooth flow. The Laplacian dissipation provides first-order-accurate smoothing in the vicinity of shock waves to reduce numerical oscillations. The set of resulting equations is integrated in time using an explicit five-stage Runge–Kutta time-stepping scheme. This scheme was designed to obtain the best balance of efficiency and robustness for viscous flows with the algebraic multigrid algorithm.

The main technique used in NSU2D to accelerate the convergence (besides local time stepping and smoothing) is the multigrid algorithm. This method accelerates convergence by damping out low-frequency errors on the coarser grids where these errors can manifest themselves as high frequencies. NSU2D uses an algebraic multigrid algorithm, as opposed to a geometric algorithm, and therefore operates on the matrix of the discrete operator, rather than on the grid of the discretization. The formulation of the algebraic algorithm can be found in Mavriplis and Venkatakrishnan.[17] Three to five grid levels were typically used for the current computations.

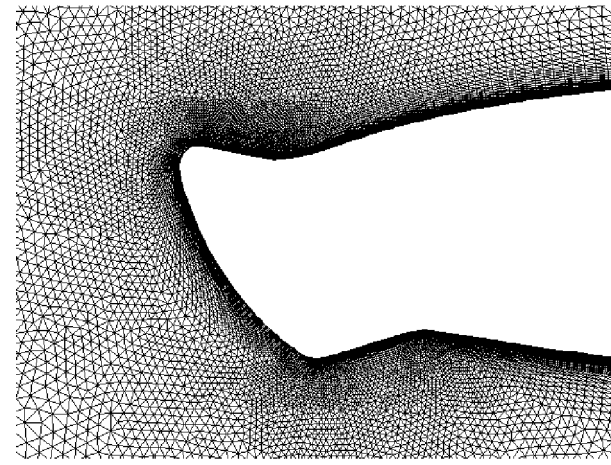

a)

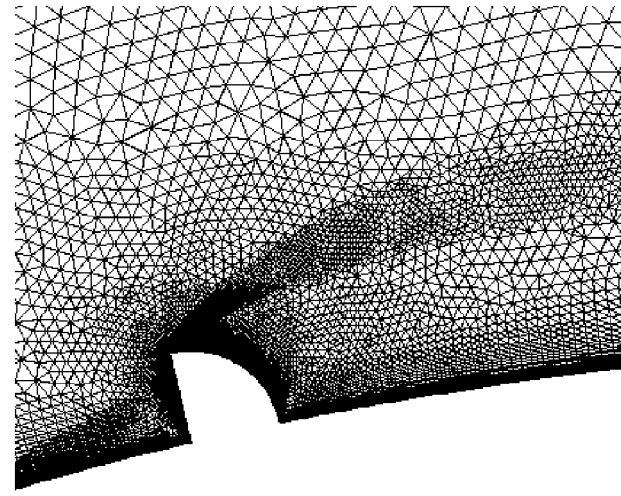

b)

Fig. 1 Unstructured grids showing close-up for: a) the leading-edge of a glazed-ice NACA 0012, b) the quarter-round ice-shape for the NACA 23012m.

The Spalart–Allmaras one-equation model[18] is used for turbulence modeling. The model is computationally local in that it does not rely on surveying the velocity or vorticity profile on a smooth grid line, roughly orthogonal to the surface.[18] It was designed and calibrated for use with mixing layers, wakes, and boundary layers. Recently, Spalart and Shur[19] modified the original Spalart–Allmaras model to account for system rotation and streamline curvature. However this alteration was found to have very little effect on the prediction of backward-facing step flows (similar to the separated flows encountered around an ice-accreted airfoil) and thus was not used. The turbulence model is integrated using a point-implicit strategy, allowing the turbulence quantities to be advanced at the same rate as the governing equations.[16]

Although the code facilitates laminar to turbulent transition, the code itself does not predict the onset of transition. Therefore, the transition points must be user specified. In this research the transition points are predicted a priori using the integral boundary-layer program of XFOIL.[20] This program incorporates an e^N-type amplification formulation for determining the transition location. To account for variations in the predicted lift of XFOIL, a lift-corrected angle of attack is used when the transition point is being computed. When comparing against experimental tests that have a boundary-layer trip placed on the airfoil, (typically at 5% chord for the upper surface and 2% for the lower surface), the transition is assumed to occur at whichever comes first: the trip location, the transition location predicted by XFOIL, or the apex of the quarter-round ice shape (when present). The latter criteria is considered because the emanating free shear layer can be considered fully developed turbulent in a small fraction of a step height downstream of the separation point for the Reynolds numbers considered herein.[21] The transition position for the lower surface was taken at the leading-edge for all negative angles of attack.

Validation with Relevant Flowfields

Before results were obtained for the upper-surface icing study, a validation study was conducted to determine the capabilities and limitations of the current computational methodology for each of the primary flow features. These validations included flat-plate boundary flows (laminar and turbulent), backstep separation flows, clean airfoils (including Reynolds-number and Mach-number effects), and a leading-edge iced airfoil flow. More details of these validations are available in Dunn and Loth[12] and Bragg and Loth.[22] To assess the accuracy of NSU2D within the viscous regions near the wall boundaries, the code was first verified for a turbulent incompressible flat-plate boundary-layer flow. The NSU2D results showed excellent agreement with data from White[23] for grid with a first transverse node spacing from the wall at a y^+ of approximately unity with a 15% successive increase in grid size away from the wall. This result was used to guide the resolution of the viscous meshes for the airfoil cases. The ability to predict separating and reattaching shear flows is also critical for accurately predicting iced-airfoil aerodynamics. The backward-facing step is a canonical geometry that provides this type of flow. The experimental data of Driver and Seegmiller[24] was used for detailed comparison by Dunn and Loth,[12] where velocity profiles and pressure distributions were reasonably reproduced. Overall, NSU2D reproduced the experimental reattachment lengths at small pressure gradients reasonably well but underpredicted the reattachment length as the expansion angle was increased.

To determine grid adaptation and prediction robustness for non-iced airfoils, the code was validated with experimental sets for clean NACA 0012 and NACA 23012 airfoils with the tunnel walls modeled directly (Dunn and Loth[12]). For the NACA 0012 airfoil the code was able to predict chord Reynolds number (Re) effects and freestream Mach number (M) effects by comparing with the data of Ladson.[25] The code also reasonably characterized the aerodynamic features up to the point of maximum lift for the clean NACA 23012 airfoil with and without a flap.[22]

The final validation was for a leading-edge glazed ice shape on the NACA 0012 airfoil, which has similar flow separation characteristics as the upper-surface iced airfoils to be investigated herein. The grid (recall Fig. 1a) contained about 60,000 nodes and used

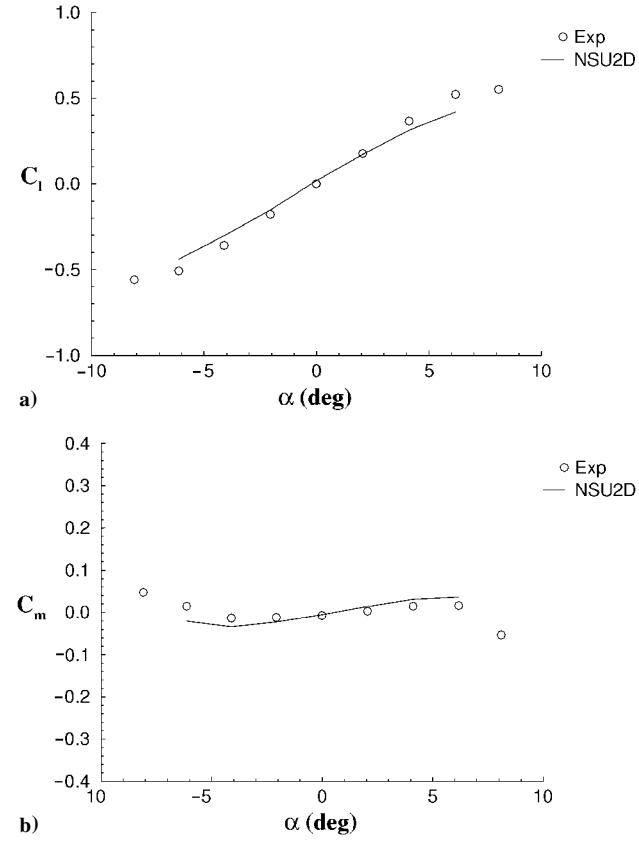

Fig. 2 Predictions and measurements for a leading-edge ice-shape on NACA 0012 shown in Fig. 1a for a) lift coefficient and b) pitching moment coefficient.

far-field conditions at the outer boundary. All runs were made at a Mach number of 0.12 and a Reynolds number of 1.5×10^6. As described in the experimental data set of Bragg,[26] the conditions probably did not have large regions of laminar flow as a result of the large and complex ice shape, and therefore turbulence was modeled over the entire airfoil surface. Potapczuk[27] found that although modeling laminar regions around the ice shape influenced the velocity profiles along the airfoil surface, simulating laminar flow did not greatly influence the integrated aerodynamic forces. This result was also found herein; therefore, modeling the entire surface as turbulent seems reasonable and appropriate. The results for this study are shown in Fig. 2 for lift and aerodynamic moment coefficients, where it can be seen that the predictions are reasonable and are similar to earlier leading-edge ice-shape predictions (discussed in the Introduction).

Results

The airfoils chosen for this study included the NACA 23012m (used in the original computational study), the NLF 0414 (which is representative of a General Aviation aircraft main wing), a business jet main wing model, and a commercial transport horizontal tailplane model. The latter two airfoils are part of the NASA Modern Airfoil program (as mentioned in the Introduction). The baseline iced-airfoil geometry was a quarter-round ice shape of size $k/c = 0.0083$, located at 10% chord on the upper surface. The commercial transport horizontal tailplane model has a negative camber to be consistent with a general tailplane orientation with upper-surface ice. All airfoils were simulated at $M = 0.2$. The business jet main wing model and the commercial transport horizontal tailplane model were run at a $Re = 8 \times 10^6$, whereas the data for $Re = 1.8 \times 10^6$ are presented for the NACA 23012m and the NLF 0414 to be consistent with the available experimental data.[22,28,29] However, it was shown that the Reynolds-number effects for all of the upper-surface iced airfoils over a range of one to eight million were negligible for the results presented herein.[22] For all simulations the tunnel walls were

modeled directly, although the experimental data and simulation data were both subsequently corrected for wall interference using the method described in Rae and Pope.[30]

Because the tunnel walls were modeled, each angle of attack required a separate grid, but only simulation data from angles that were fully computationally converged are reported in the figures. The initial grids contained approximately 100,000 nodes and 1300 points along the airfoil surface. The grid points were clustered around the ice shape and within the separation region. The spacing of the first grid point normal to the airfoil surface was 10^{-6} chord lengths with a 15% successive increase in grid size away from the wall. This grid was then adapted using the procedure described earlier. The final grids contained approximately 125,000 nodes.

For the clean conditions the four airfoils considered for the study have distinct loading distributions. These can be illustrated by comparing pressure distributions for an equivalent lift of the noniced condition. Figures 3a–3d show the surface pressure distribution for the clean case for all of the four airfoils at an equivalent C_ℓ of approximately 0.5. The NACA 23012m is a forward-loaded airfoil with a light loading of the flap. The NLF 0414 has a relatively uniform chordwise loading until the pressure recovery near the trailing edge. Both the business jet main wing model and the commercial transport horizontal tailplane model have the same type of loading; both are forward-loaded airfoils with large suction peaks and a light loading of the flap in the clean case.

For iced conditions the differences in loading for these four airfoils can be illustrated by examining the flowfields for an equivalent lift, ice-shape location ($x/c = 0.1$), and size ($k/c = 0.0083$) shown in Figs. 4–7. The streamlines and the pressure distribution for all of the four airfoils were considered for an equivalent $C_\ell = 0.26$. The iced NACA 23012m has the largest bubble with the reattachment point close to the trailing edge. The NLF 0414 and the business jet main wing model have smaller separation with reattachment points close to $x/c = 0.27$, and the commercial transport horizontal tailplane model has a reattachment point at $x/c = 0.34$. The business jet main wing model and the commercial transport horizontal tailplane model exhibit very similar C_p profiles in both clean and iced case, despite the negative camber of the latter. In general, the pressure distributions are predicted reasonably well for the NACA 23012m and the NLF 0414 airfoils.[22] The comparisons in the resulting aerodynamic forces between airfoils will be discussed at the end of the results section. In the following presentation of force coefficients for the individual airfoils, the lift and hinge-moment distributions will be generally shown because their influence in aerodynamic control in icing conditions is paramount. For conciseness, the figures for drag and pitching moment coefficients are not generally shown, but are available in Bragg and Loth.[22]

NACA 23012m Airfoil

Analysis of the aerodynamic coefficients, reattachment lengths, pressure distributions, and flowfield plots[12,22] for the NACA 23012m iced case indicates three general regimes of flow phenomena, which can be isolated to aid in future discussion: linear, nonlinear, and fully separated. These regimes are illustrated by the separation bubble size plotted in Fig. 8 for the baseline ice-shape geometry. The linear regime is associated with low angles of attack (approximately less than 0 deg in the experimental case and less than −2 deg in the computational case). Here the separation bubble remains close to the airfoil surface, and the chordwise growth of the bubble as the angle of attack is increased is fairly slow. At higher angles of attack (up to 4 or 5 deg), a nonlinear regime occurs where there is a break in the aerodynamic forces and moments. Here the bubble displays rapid growth over a relatively small range of angle of attack where unsteady flow becomes significant. Once the separation region reaches the trailing edge, the airfoil is in the fully separated regime, $\alpha > 4$ deg. Here the bubble quickly begins to extend away from the airfoil and into the outer flowfield. With this type of bubble, large-scale vortex shedding occurs as measured by Bragg and Gurbacki.[31] This type of unsteady phenomenon cannot be captured with the current steady-state computational strategy, and therefore the computational results are questionable at these

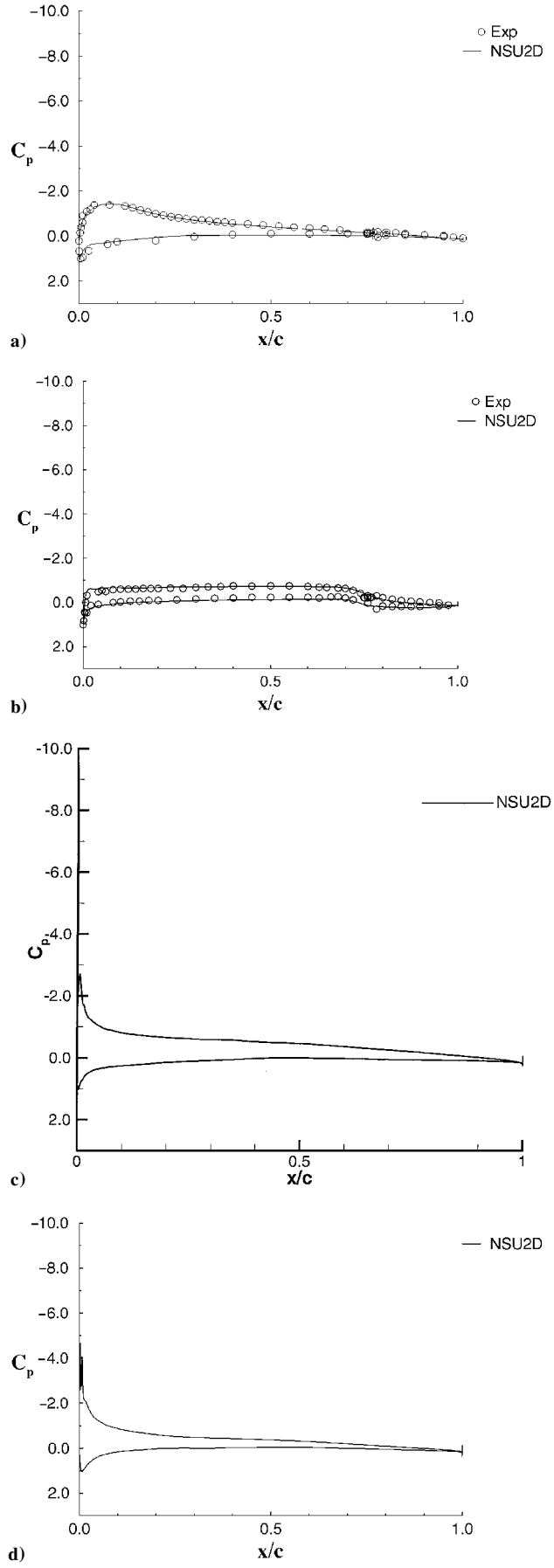

Fig. 3 Surface pressure distribution for non-iced ($k/c = 0.00$) condition for an equivalent C_ℓ = 0.5 for a) NACA 23012m at α = 4 deg, b) NLF 0414 at α = 0 deg, c) business jet main wing model at α = 4 deg and d) commercial transport horizontal tailplane model at α = 4 deg.

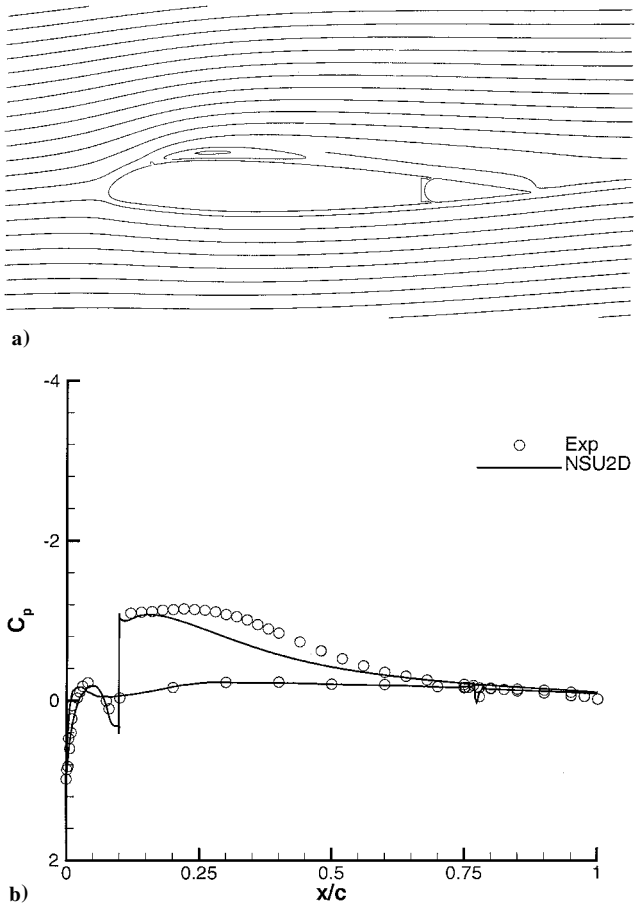

Fig. 4 a) Streamlines and b) surface pressure distributions for a NACA 23012m with k/c = 0.0083 quarter-round ice shape located at x/c = 0.1 and α = 3 deg.

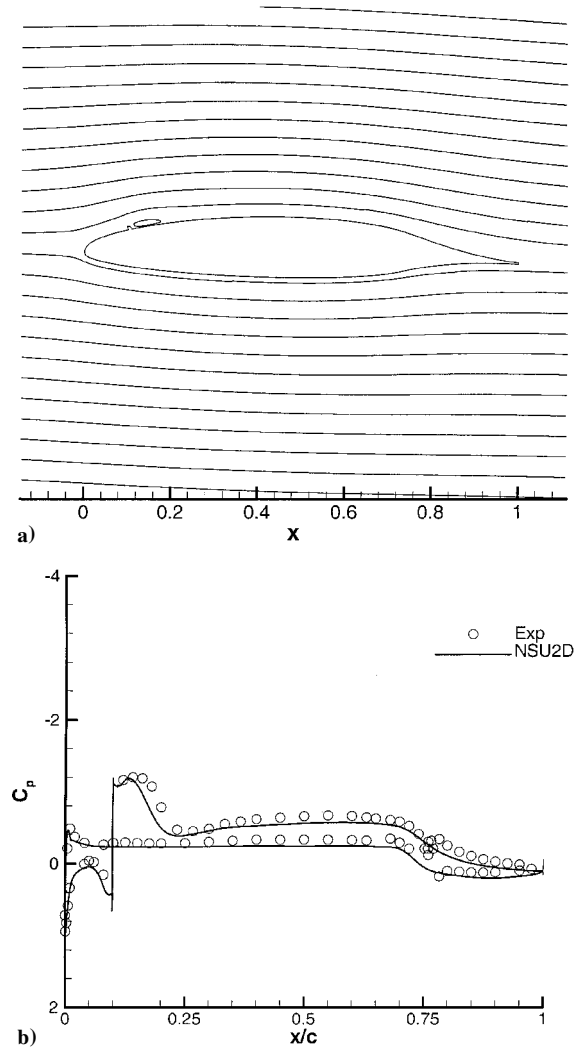

Fig. 5 a) Streamlines and b) surface pressure distributions for a NLF 0414 airfoil with k/c = 0.0083 quarter-round ice shape located at x/c = 0.1 and α = 2 deg.

angles. In the following, the aerodynamic influence of a quarter-round ice shape is considered by varying its maximum height. The ice location was held constant at 10% chord, and two sizes were studied: $k/c = 0.0083$ and 0.0139. In addition, a case with no ice shape ($k/c = 0.0$) but a boundary-layer trip was used as a reference condition.

The lift curves for these configurations are shown in Fig. 9a. The significant reduction in lift curve slope and the dramatic reductions in maximum lift coefficient and maximum-lift angle caused by the ice-shape presence were predicted reasonably well by NSU2D. However, for both iced cases the NSU2D predictions exhibited a weaker, although more abrupt, break in the lift curve slope than that shown by the experiments. Although no noticeable maximum lift condition was seen in the NSU2D predictions, the break in the lift curve slope can be used to estimate the trends for loss in maximum lift. Here the break does occur at an earlier angle for the larger ice-shape case (at $\alpha = 1$ deg) than for the smaller ice-shape case (at $\alpha = 3$ deg), which corresponds well with the start of the experimental breaks.

Figure 9b shows the drag predictions. The trends caused by the presence and height change of the ice shape were well predicted by NSU2D considering the large amount of separation occurring for the iced airfoil flows. At low angles of attack, NSU2D predicted the small increase in drag as the ice size was increased, although the magnitude was slightly underpredicted. Both the computations and the experiments showed a significant increase in drag for the iced cases at large angles of attack. However, unlike the clean case, the large increases in drag for the iced cases occurred a couple of degrees before the maximum lift point.

Figure 9c shows the pitching-moment coefficient distribution with angle of attack. The trends caused by the presence of the ice shapes were well reproduced by NSU2D. In fact, the NSU2D results for the iced cases had better agreement with the experiments than the clean case (perhaps because of the decrease in flow through the flap gap). NSU2D performed remarkably well for predicting the strong drop-off in moment at positive angles of attack as the ice shape was increased in size. However, the computations did not predict the subsequent increase in moment coefficient seen in the experimental data for angles past stall.

Perhaps the most important aerodynamic coefficient with respect to aircraft control is the hinge-moment. The comparison between computation and experiment of this critical parameter is shown in Fig. 9d. Again NSU2D successfully predicted the qualitative trends resulting from the presence and change in height of the ice shape. In particular the increased drop-off in C_h at high angles of attack was reproduced both qualitatively and quantitatively. The predicted pressure distribution[12,22] for each of the three configurations at $\alpha = 3$ deg also matched well with the experimental data. The distribution showed that the presence of the ice shape caused an increase in pressure at the leading edge, i.e., the suction peak was reduced. This created a much more aft-loaded airfoil with a subsequent change in the pitching-moment and loss in lift. Also, the pressure along the lower surface decreased as the ice-shape size was increased, resulting in a further loss in lift.

The effect on the lift and hinge-moment coefficients caused by a quarter-round ice shape of size $k/c = 0.0083$ located at 10, 20, and 30% chord is shown in Figs. 10a and 10b. Generally, the computational results agreed well with the experimental data for angles of attack within the linear range. For the three locations tested the 10% chord location had the strongest influence on the aerodynamic characteristics of the airfoil, in particular it resulted in the largest

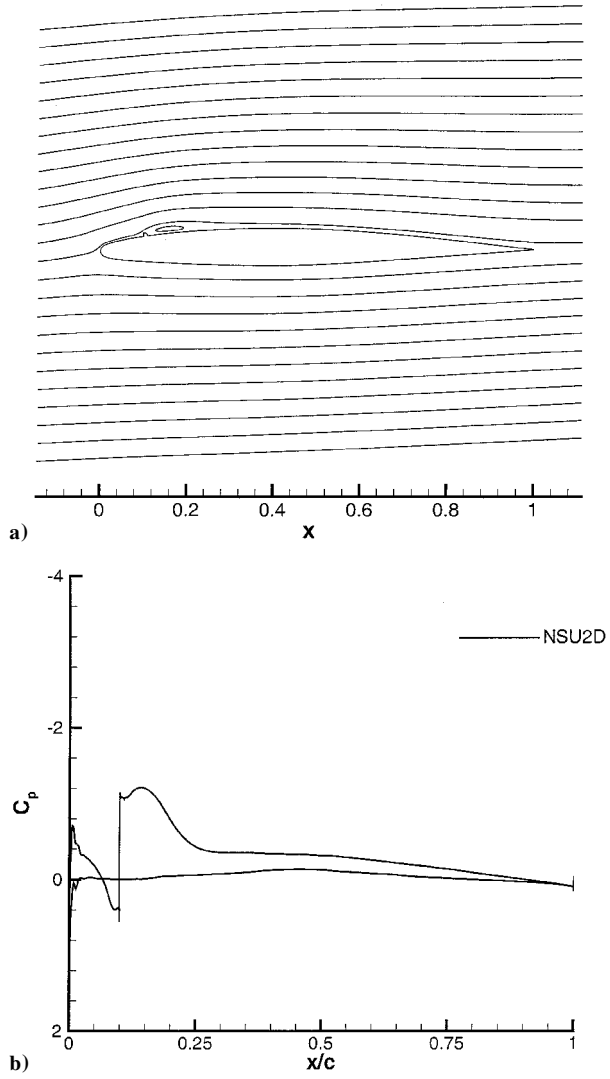

Fig. 6 a) Streamlines and b) surface pressure distributions for a business jet main wing model airfoil with k/c = 0.0083 quarter-round ice-shape located at x/c = 0.1 and α = 2.

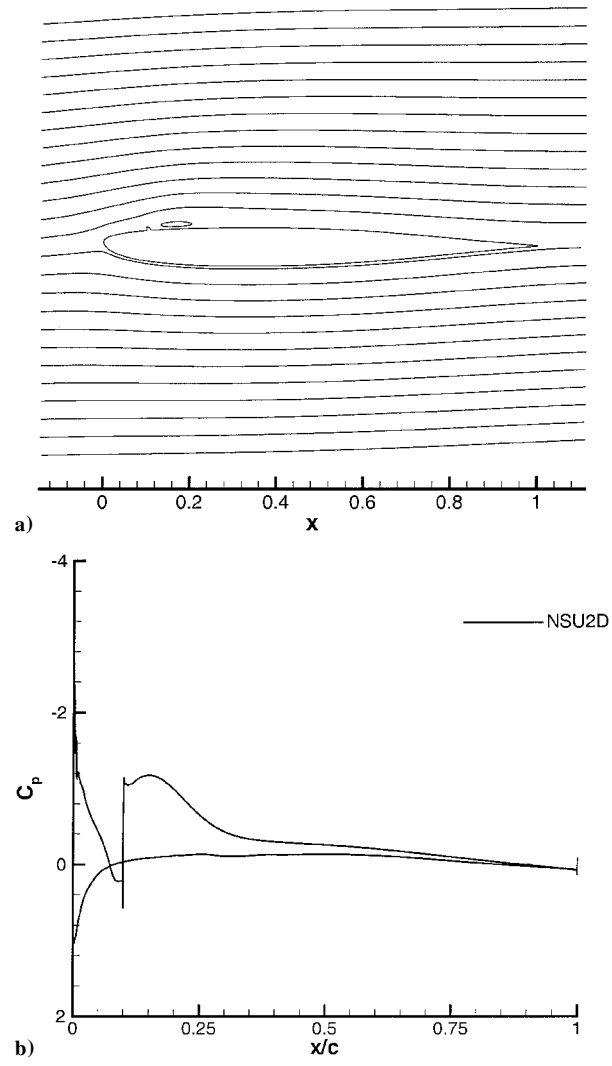

Fig. 7 a) Streamlines and b) surface pressure distributions for a commercial transport horizontal tailplane model with k/c = 0.0083 quarter-round ice shape located at x/c = 0.1 and α = 3 deg.

reduction in lift curve slope through the linear range. The 10% chord location was also the first to experience the break in the lift curve, indicating the earliest stall (although the computations did not predict the actual stall) and yielded the highest drag predictions. As the ice shape was moved rearward on the airfoil, the hinge-moment curves displayed a much more gradual break, which is desirable for aircraft control.

Figure 11 displays the pressure distribution along the airfoil surface at $\alpha = 3$ deg for the three ice-shape locations. As expected, the separation region not only followed the ice shape as it moved rearward but also was seen to decrease in overall extent. The airfoil with the ice shape at 10% chord did not display a suction peak at the leading-edge, whereas the geometries with the ice shape moved farther back did possess a peak (although not as large as in the clean case, e.g., Fig 3a). This appears to be the reason why the 10% chord location produced the greatest decrease in lift as well as the strongest influence on the moment coefficients. Figure 12 plots the C_ℓ when the flow first becomes fully separated vs the location of simulated ice accretion. We see that the most detrimental effect on the lift occurs close to the 10% location as also seen from the C_ℓ–α curve. This is consistent with the experimental results,[22] which noted a critical location of 12% (also shown in the figure).

To investigate the influence of flap deflection, calculations for the clean NACA 23012m airfoil were first studied for the flap deflections of 0, 5, and 10 deg (Figs. 13a and 13b) for both computational predictions and experimental data. The NSU2D predictions

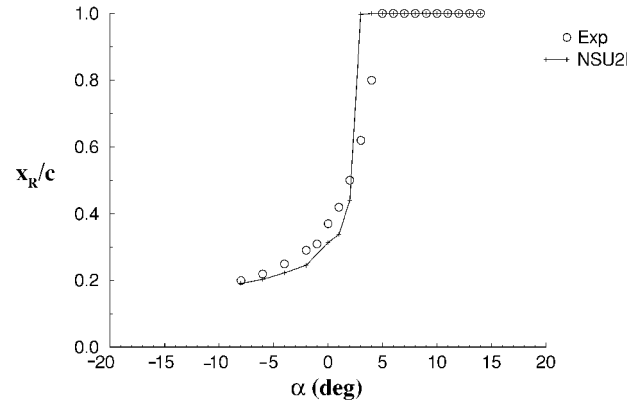

Fig. 8 Reattachment locations of the separation bubble for the NACA 23012m with k/c = 0.0083 for quarter-round ice shape at x/c = 0.1.

for the noniced cases exhibit good comparison with the experimental results, although the slope of the lift curve and maximum lift coefficient were overestimated. The experimental uncertainty in lift was limited to 0.33%. The influence of flap deflection on the airfoils with the ice shape is shown in Figs. 14a and 14b, where the curves are shifted with the flap deflection but are not qualitatively changed. For the lift there is a break at about 3 deg, which is maintained as the flap deflection increases, indicating that it is the onset of full

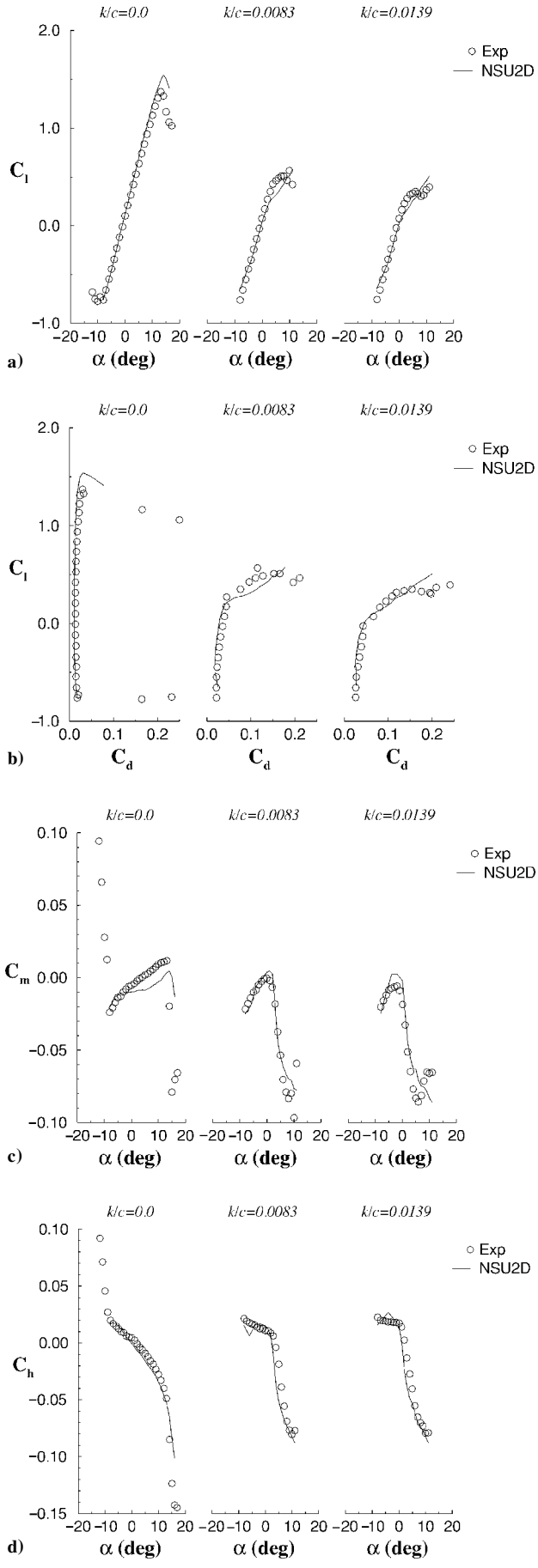

Fig. 9 Effect of ice-shape height for a NACA 23012m at x/c = 0.1 on a) lift coefficient, b) drag coefficient, c) pitching-moment coefficient, and d) hinge-moment coefficient. Note: k/c = 0.00 is the clean case.

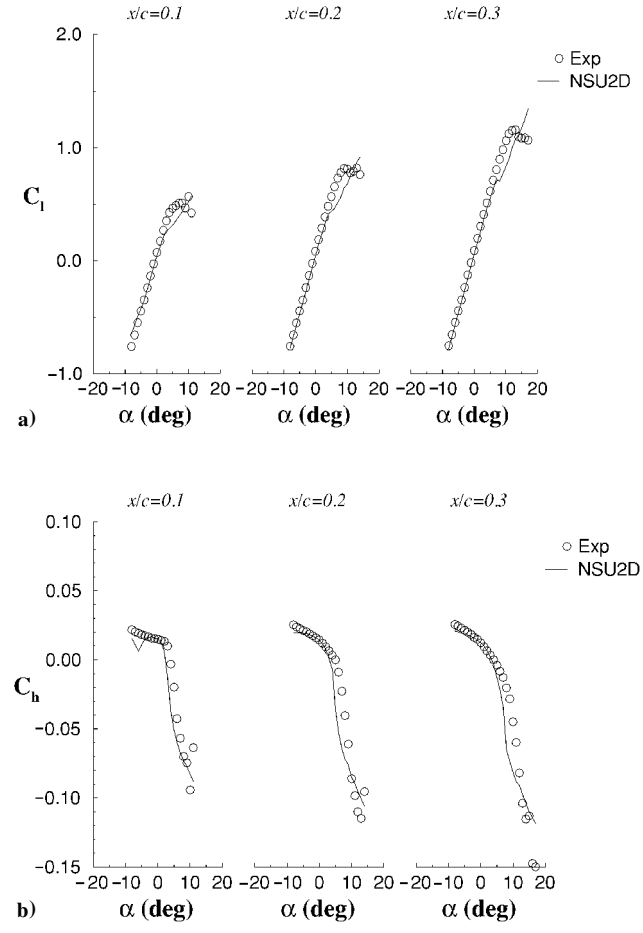

Fig. 10 Effect of ice-shape location for a NACA 23012m for k/c = 0.0083 on a) lift coefficient and b) hinge-moment coefficient.

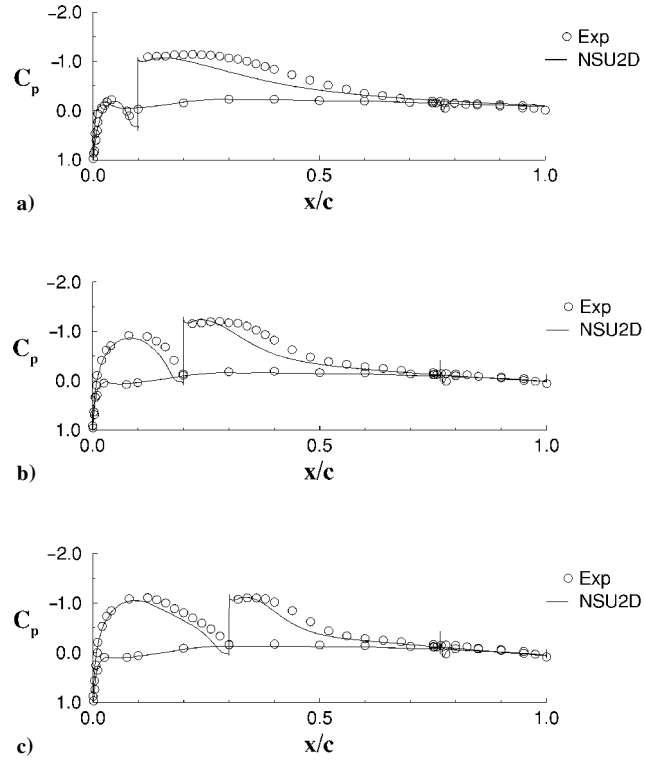

Fig. 11 Effect of ice-shape location on pressure distribution of a NACA 23012m at α = 3 deg and k/c = 0.0083 for ice-shape located at x/c: a) = 0.1, (b) = 0.2, and (c) 0.3.

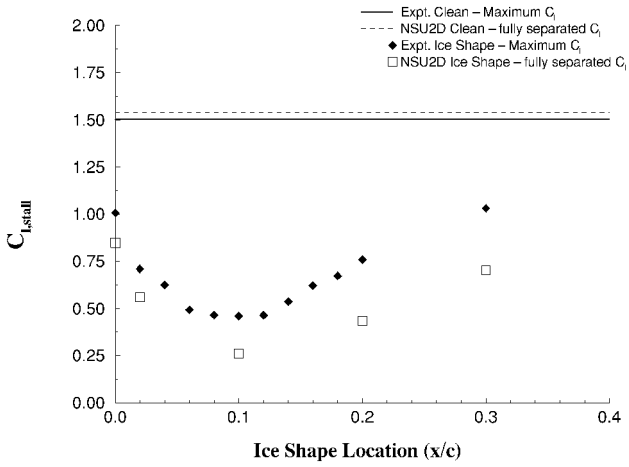

Fig. 12 Lift coefficient for angle of attack at which flow first fully separates vs. *x/c* for a NACA 23012m airfoil with *k/c* = 0.0083 quarter-round ice shape.

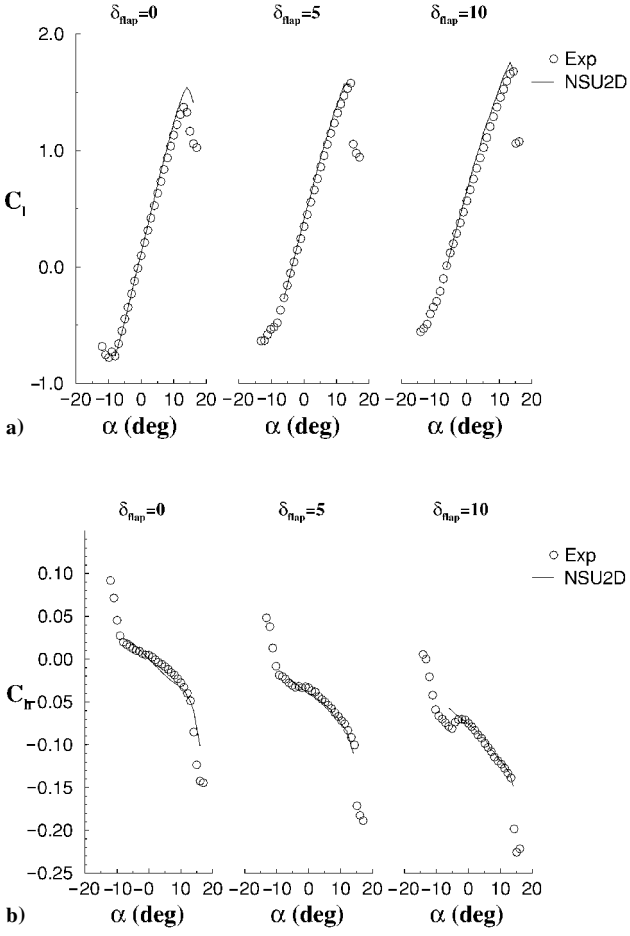

Fig. 13 Effect of flap deflection for a NACA 23012m with *k/c* = 0.00 (clean) on a) lift coefficient and b) hinge-moment coefficient.

upper-surface flow separation that leads to poor lift prediction and not the onset of increased overall lift or circulation. Similarly, the predictive performance is approximately independent of flap deflection angle for the drag, aerodynamic moment, and hinge-moment curves, although for the latter the hinge-moment break is not as sharp (Fig. 14b).

NLF 0414 Airfoil

Figures 15a–15d show the effect on the lift, drag, pitching-moment, and hinge-moment coefficients as a result of variation in

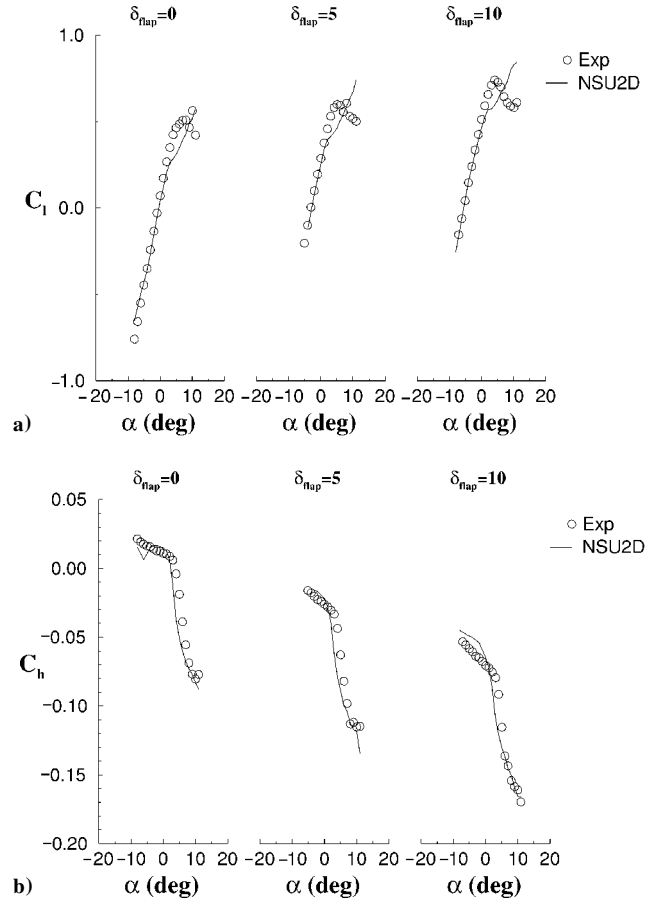

Fig. 14 Effect of flap deflection on hinge-moment coefficient for a NACA 23012m with ice-shape of height *k/c* = 0.0083 and located at *x/c* = 0.1 on a) lift coefficient and b) hinge-moment coefficient.

ice-shape location for the NLF 0414 airfoil with quarter-round ice shape of size $k/c = 0.0083$ at $x/c = 0.02, 0.1$ and 0.3. Both the computations and experiments indicate large detrimental effects for all of the ice-shape locations tested, but the location close to the leading-edge appears to be the most severely affected. The prediction of lift (Fig. 15a) is reasonable up until full separation after which it significantly underpredicts the lift and does a poor job of predicting the maximum C_ℓ. Similarly, the predicted drag coefficients (Fig. 15b) indicated good agreement with the experimental results at low angles of attack, but the angle at which the drag suddenly increases was underpredicted (especially for $x/c = 0.1$).

The break in the pitching-moment curve (Fig 15c) occurred earlier for the computations. This could be because the bubble reattached earlier, compared to the experiment. However, the hinge-moment predictions (Fig. 15d) agreed well with experimental results, although a distinctive break was observed in the computational predictions of hinge moment of $x/c = 0.02$ case, which was substantially delayed in the experimental results. A study of size variation[22] for this airfoil noted that the larger ice-shape size had a more detrimental effect (as expected).

Figure 16 plots the C_ℓ when the flow becomes first fully separated vs the location of simulated ice accretion for the NLF 0414 airfoil. Both computations and experiments indicate that for $k/c = 0.0083$ the near leading-edge locations, e.g., $x/c = 0.02$, have the most detrimental effect. All of the locations tested seem to have a significant detrimental effect compared to the clean case.

Business Jet Main Wing Model Airfoil

The effect of ice-shape location on aerodynamic coefficients for the $k/c = 0.0083$ ice shape on the business jet main wing model airfoil was similarly investigated. It was observed from the lift and drag plots that the most detrimental effect of the ice shape on lift and drag would occur if the ice shape was placed close to $x/c = 0.02$

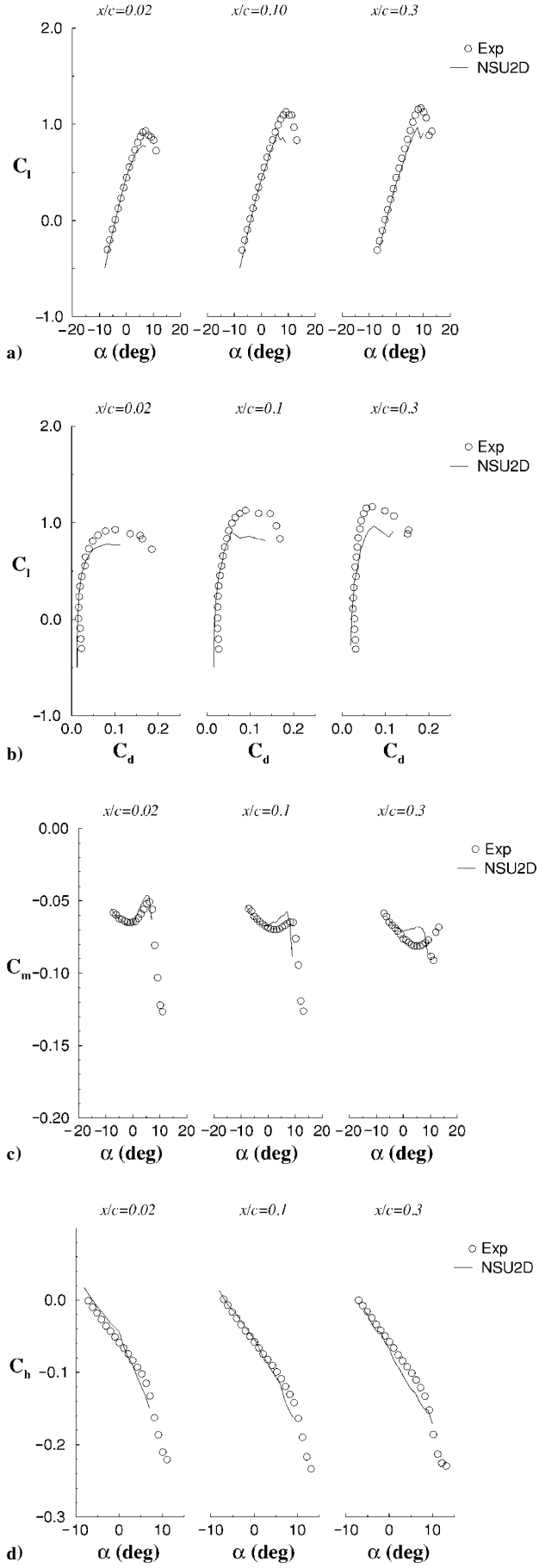

Fig. 15 Effect of ice-shape location for $k/c = 0.0083$ for the NLF airfoil on a) lift coefficient, b) drag coefficient, c) pitching-moment coefficient, and d) hinge-moment coefficient.

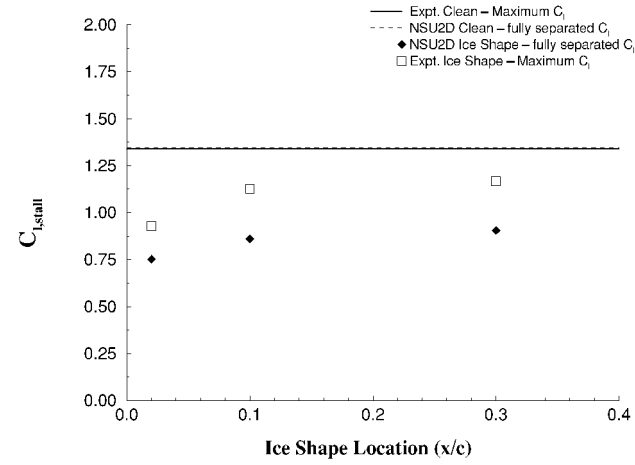

Fig. 16 Lift coefficient for angle of attack at which flow first fully separates vs x/c for a NLF 0414 airfoil with $k/c = 0.0083$ quarter-round shape.

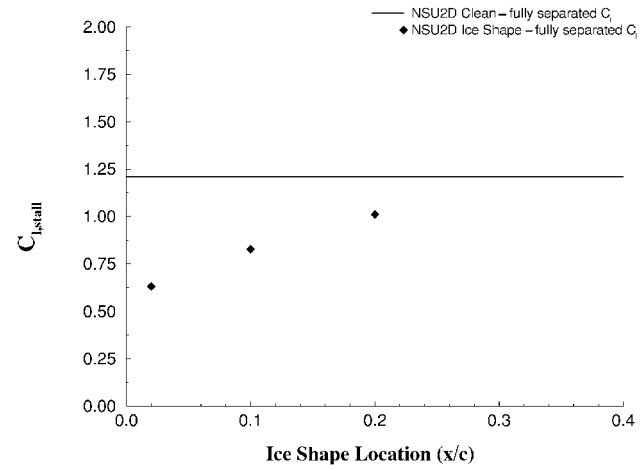

Fig. 17 Lift coefficient for angle of attack at which flow first fully separates vs x/c for a business jet main wing model airfoil with $k/c = 0.0083$ quarter-round ice shape.

(e.g., Fig. 17). This is close to the general location of minimum pressure for this airfoil in clean conditions (Fig. 3c). Based on streamline contours, the $x/c = 0.02$ iced case exhibits a combination of thin airfoil type of stall and trailing-edge type of stall, wherein the trailing-edge separation point moves closer to and merges with the reattachment point of the bubble.

Comparison of the Four Airfoils

The effect on the aerodynamic coefficients caused by variation in airfoil geometry was studied by comparing the NACA 23012m, NLF 0414, business jet main wing model, and commercial transport horizontal tailplane airfoil geometries with a quarter-round ice shape of size $k/c = 0.0083$ located at 10% chord. The $x/c = 0.1$ was chosen because it has been shown herein to have a substantial impact on performance.

Figures 18a and 18b show the lift and hinge-moment coefficients of the four airfoils with the available experimental data, and results for drag and pitching-moment are available in Bragg and Loth.[22] For the lift and drag the effects of the ice-shape simulation were much more severe on the NACA 23012m than on the NLF 0414. This can be attributed to the large differences in their clean model pressure distributions. The clean NACA 23012m is a very forward-loaded airfoil, with a very large leading-edge suction peak. The NLF 0414 has a relatively uniform chordwise loading until the pressure recovery near the trailing edge. On the NACA 23012m the largest penalties occurred when the simulated ice shape prevented the leading-edge suction peak from forming. On the NLF 0414 it was found that all of

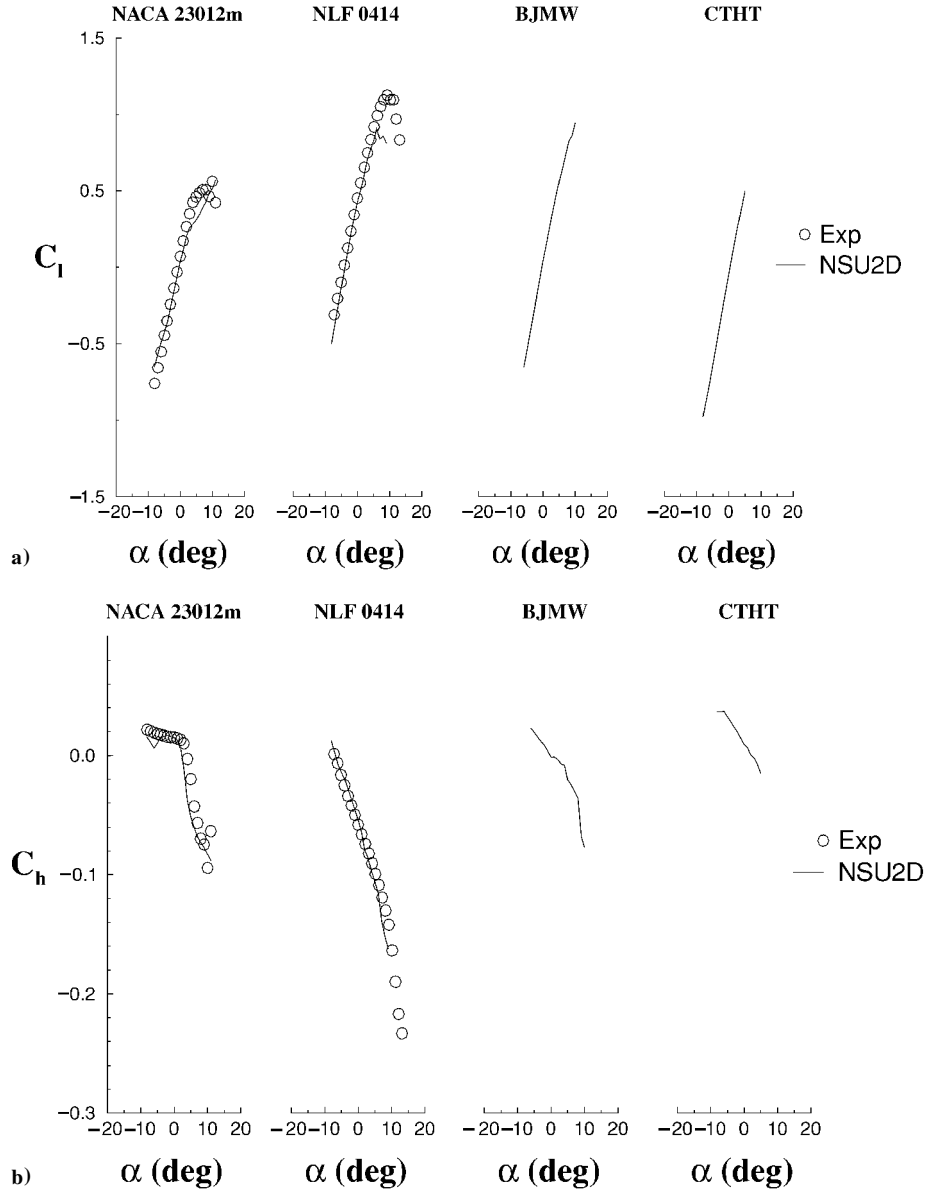

Fig. 18 Effect of airfoil geometry for k/c = 0.0083 ice-shape located at x/c = 0.1 on a) lift coefficient and b) hinge-moment coefficient. Airfoils include NACA 23012m, NLF 0414, business jet main wing model (BJMW) and commercial transport horizontal tailplane model (CTHT).

the locations had detrimental effect on the aerodynamic parameters, but the sensitivity to location was not as strong. The business jet main wing model and the commercial transport horizontal tailplane airfoils (both forward loaded in clean conditions) exhibit similar iced aerodynamic performance, although there is a shift owing to the differences in camber, which was also observed in the clean cases.[22]

The ice shape affected the hinge moment much more on the NACA 23012m than on the NLF 0414. The reason stems from the fact that on the clean NACA 23012m the flap is lightly loaded. When the separation bubble caused by the ice shape reached the flap, the flap became heavily loaded and caused a large change in the hinge-moment slope. On the NLF 0414 the flap was heavily loaded even on the clean model caused by early flap separation. Thus, even when the bubble reached the flap, it did not alter the C_h. The flap loading was very light in the clean case of the business jet main wing model, and the loading increased greatly when the separation bubble reached the flap causing breaks in the hinge-moment curve, which were not observed in the case of NLF 0414 airfoil. In the case of commercial transport horizontal tailplane airfoil, there was trailing-edge separation even at very low angles of attack; hence, the bubble did not dramatically change the slope of the hinge-moment curve. And none of the airfoils displayed as strong a hinge-moment break as was found on the NACA 23012m.

Conclusions

The present computational formulation qualitatively predicts the experimental trends of the major aerodynamic forces and moments associated with the simulated ice-shape presence (with and without flap deflection). As in the experiments, the simulated upper-surface ice-shape airfoils produced a large separation bubble, drastically changed the airfoil pressure distributions, and modified the airfoil from leading edge to thin-airfoil stall. In addition, hinge moments, pressure distributions, and reattachment lengths were also reasonably correlated with experimental results. However, the lift force was not well predicted once the upper surface was fully separated, which was attributed to the highly unsteady vortex shedding at this condition.

The NACA 23012m exhibited the strongest lift degradation at $x/c = 0.1$, which was attributed to the absence of the suction peak near the leading-edge. The more uniformly loaded NLF 0414 airfoil did not exhibit a distinctive critical ice-shape location, i.e., the lift loss at fully separated conditions was roughly the same for x/c

values ranging from 0.02 to 0.3. The most critical ice-shape location for the business jet main wing model and commercial transport horizontal tailplane model airfoils with upper-surface ice shapes was very close to the leading edge around $x/c = 0.02$. This is attributed to a large decrease in the pressure suction peak at the leading-edge for these airfoils, which are highly forward-loaded and have high suction peaks in clean conditions. Finally, Reynolds number effects were negligible for all the ice-shape cases (unlike for the clean airfoils).

Acknowledgments

This work was sponsored by the Federal Aviation Administration (FAA) under Grant DTFA MB96-6-023 with James Riley (of the FAA) as Technical Monitor and Mike Bragg (of University of Illinois at Urbana–Champaign) as the grant director. The computations were completed under a grant from the National Center for Supercomputing Allocations. We wish to also thank Gene Addy of NASA's John H. Glenn Research Center at Lewis Field for providing us with the airfoil geometries of the preceding airfoils. We would also like to acknowledge assistance from (alphabetically) Tom Bond, Tim Dunn, Sam Lee, Dimitri Mavriplis, and Mark Potapczuk.

References

[1]National Transportation Safety Board, "Icing Tanker Test Factual Report," Docket No: SA-512, Exhibit No: 13B, DCA95MA001, Washington, DC, 16 Feb. 1995.

[2]Addy, H. E., Jr., and Miller, D. R., "A Study of Large Droplet Ice Accretion in the NASA Lewis IRT at Near-Freezing Conditions; Part 2," NASA TM 107424, May 1996.

[3]Potapczuk, M. G., and Gerhart, P. M., "Progress in Development of a Navier–Stokes Solver for Evaluation of Iced Airfoil Performance," AIAA Paper 85-0410, Jan. 1985.

[4]Potapczuk, M. G., "Numerical Analysis of a NACA0012 Airfoil with Leading Edge Ice Accretions," AIAA Paper 87-0101, Jan. 1987.

[5]Baldwin, B. S., and Lomax, H. J., "Thin Layer Approximation and Algebraic Model for Separated Turbulent Flows," AIAA Paper 78-0257, Jan. 1978.

[6]Caruso, S. C., and Farschi, M., "Automatic Grid Generation for Iced Airfoil Flowfield Predictions," AIAA Paper 92-0415, Jan. 1992.

[7]Dompierre, J., Cronin, D. J., Bourgault, Y., Baruzzi, G. S., Habashi, W. G., and Wagner, G. A., "Numerical Simulation of Performance Degradation of Ice Contaminated Airfoils," AIAA Paper 97-2235, June 1997.

[8]Kwon, O. J., and Sankar, L. N., "Numerical Study of the Effects of Icing on Finite Wing Aerodynamics," AIAA Paper 90-0757, Jan. 1990.

[9]Wright, W. B., and Potapczuk, M. G., "Computational Simulation of Large Droplet Icing," *Proceedings of the Federal Aviation Administration International Conference on Aircraft Inflight Icing*, Vol. II., DOT/FAA/AR-96/81,II, FAA, Washington, DC, Aug. 1996, pp. 545–555.

[10]Bragg, M. B., "Aircraft Aerodynamic Effects Due to Large Droplet Ice Accretions," AIAA Paper 96- 0932, Jan. 1996.

[11]Bragg, M. B., "Aerodynamics of Supercooled-Large-Droplet Ice Accretion and the Effect on Aircraft Control," *Proceedings of the Federal Aviation Administration International Conference on Aircraft Inflight Icing*, Vol. II., DOT/FAA/AR-96/81,II, FAA Washington, DC, Aug. 1996, pp. 387–399.

[12]Dunn, T. A., Loth, E., and Bragg, M. B., "A Computational Investigation of Simulated Large-Droplet Ice Shapes on Airfoil Aerodynamics," *Journal of Aircraft*, Vol. 36, No. 5, 1999, pp. 836–843.

[13]Addy, H. E., Jr., "Ice Accretions and Icing Effects for Modern Airfoils," NASA/TP-2000-210031, DOT/FAA/AR-99/89, April 2000.

[14]Mavriplis, D., "A CFD Package for Multi-Element Airfoil High-Lift Analysis (Revision 4)," *Scientific Simulations*, Dec. 1996.

[15]Pirzadeh, S., "Unstructured Viscous Grid Generation by the Advancing-Layers Method," *AIAA Journal*, Vol. 32, No. 8, 1994, pp. 1735–1737.

[16]Mavriplis, D., "Multigrid Solution of Compressible Turbulent Flow on Unstructured Meshes Using a Two-Equation Model," NASA CR-187513, Jan. 1991.

[17]Mavriplis, D., and Venkatakrishnan, S., "Agglomeration Multigrid for Two-Dimensional Viscous Flows," *Computers and Fluids*, Vol. 24, No. 5, 1995, pp. 553–570.

[18]Spalart, P. R., and Allmaras, S. R., "A One-Equation Turbulence Model for Aerodynamic Flows," AIAA Paper 92-0439, Jan. 1992.

[19]Spalart, P. R., and Shur, M., "On the Sensitization of Turbulence Models to Rotation and Curvature," *Aerospace Science and Technology*, Vol. 1, No. 5, 1997, pp. 297–302.

[20]Drela, M., "XFOIL 6.6 User Primer," Massachusetts Inst. of Technology, Aero. and Astro. Engineering, Cambridge, MA, March 1996.

[21]Oakley, T., Loth, E., and Adrian, R., "Cinematic Particle Image Velocimetry of a Turbulent Free Shear Layer," *AIAA Journal*, Vol. 34, No. 2, 1996, pp. 299–308.

[22]Bragg, M., and Loth, E., "Effect of Large-Droplet Ice Accretion Shapes on Airfoil and Wing Aerodynamics and Control," Dept. of Aeronautical and Astronautical Engineering, Univ. of Illinois at Urbana—Champaign, Federal Aviation Administration Contractor Rept. DOT/FAA/AR-00/14, April 2000.

[23]White, F. M., *Viscous Fluid Flow*, 2nd Ed., McGraw–Hill, New York, 1991, pp. 415–433.

[24]Driver, D. M., and Seegmiller, H. L., "Features of a Reattaching Turbulent Shear Layer in Divergent Channel Flow," *AIAA Journal*, Vol. 23, No. 2, 1985, pp. 163–171.

[25]Ladson, C. L., "Effects of Independent Variation of Mach and Reynolds Numbers on the Low-Speed Aerodynamic Characteristics of the NACA 0012 Airfoil Section," NASA TM-4074, 1988.

[26]Bragg, M., "An Experimental Study of the Aerodynamics of a NACA 0012 Airfoil with a Simulated Glaze Ice Accretion, Vol. II," NASA CR-191007, March 1993.

[27]Potapczuk, M., "Numerical Analysis of a NACA0012 Airfoil with Leading Edge Ice Accretions," AIAA Paper 87-0101, Jan. 1987.

[28]Lee, S., Dunn, T., Gurbacki, H. M., Bragg, M. B., and Loth, E., "An Experimental and Computational Investigation of Spanwise-Step-Ice Shapes on Airfoil Aerodynamics" AIAA 98-0490, Jan. 1998.

[29]Lee, S., and Bragg, M. B., "Effects of Simulated-Spanwise Ice Shapes on Airfoils: Experimental Investigation" AIAA 99-0092, Jan. 1999; also published as "Experimental Investigation of Simulated Large-Droplet Ice Shapes on Airfoil Aerodynamics" *Journal of Aircraft*, Vol. 36, No. 5, 1999, pp. 840–850.

[30]Rae, W. H., and Pope, A., *Low-Speed Wind Tunnel Testing*, Wiley, New York, 1984.

[31]Bragg, M. B., and Gurbacki, H., "Sensing Aircraft Icing Effects by Flap Hinge Moment Measurement," AIAA Paper 99-3149, June–July 1999.